



FULL LENGTH ARTICLE

A novel aptamer-based small RNA delivery platform and its application to cancer therapy

Toshihiko Tanno ^{a,b}, Peng Zhang ^b, Christopher Bailey ^b,
Yin Wang ^b, Wannaporn Ittiprasert ^c, Martin Devenport ^a,
Pan Zheng ^{a,b,**}, Yang Liu ^{a,b,*}

^a OncoC4, Inc., Rockville, MD 20850, USA

^b Division of Immunotherapy, Institute of Human Virology, University of Maryland School of Medicine, Baltimore, MD 21201, USA

^c Department of Microbiology, Immunology and Tropical Medicine, School of Medicine and Hygiene, George Washington University, NW Washington, DC 20037, USA

Received 22 April 2022; accepted 4 May 2022

Available online 20 May 2022

KEYWORDS

Aptamer;
Cancer;
Micellar nanoparticle;
miRNA;
Target delivery

Abstract Major challenges such as nuclease degradation, rapid renal clearance, non-specific delivery, poor cellular uptake and inflammatory response have limited the clinical application of small RNA-mediated gene silencing. To overcome these challenges, we designed a novel targeting small RNA delivery platform comprising of three oligonucleotides: (1) a guide RNA sequence, (2) part of a passenger sequence linked to a DNA aptamer via a PEG linker, and (3) another passenger sequence conjugated to cholesterol, which assemble through complementary base pair annealing. Remarkably, in the presence of magnesium, this molecule self-assembled into a nanoparticle with a hydrophobic cholesterol core, hydrophilic RNA oligonucleotide shell and PEG-linked DNA aptamer flare. The nanoparticles conferred protection to the RNA oligonucleotides against nuclease degradation, which increased bioavailability, and reduced systemic inflammatory responses. The aptamer allowed targeted delivery of RNA therapeutics through cell-specific surface markers, and once inside the cell, the nanoparticles induced lysosomal leakage that released the RNA oligonucleotides into the cytosol to achieve

Abbreviations: AF, Alexa Fluore; CMC, critical micelle concentration; IVIS, *in vivo* fluorescence imager; MEF, mouse embryonic fibroblast cell line.

* Corresponding author. OncoC4, Inc., 9640 Medical Center Drive, Rockville MD, 20850, USA.

** Corresponding author. OncoC4, Inc., 9640 Medical Center Drive, Rockville MD, 20850, USA.

E-mail addresses: pzheng@oncoc4.com (P. Zheng), yangl@oncoc4.com (Y. Liu).

Peer review under responsibility of Chongqing Medical University.

<https://doi.org/10.1016/j.gendis.2022.05.004>

2352-3042/© 2022 The Authors. Publishing services by Elsevier B.V. on behalf of KeAi Communications Co., Ltd. This is an open access article under the CC BY-NC-ND license (<http://creativecommons.org/licenses/by-nc-nd/4.0/>).

gene silencing. We created a c-Kit-targeting miR-26a delivery particle that specifically accumulated in c-Kit⁺ breast cancer, significantly increased T cell recruitment, and inhibited tumor growth. Regression of large established tumors were achieved when the nanoparticle was used in combination with anti-CTLA-4 monoclonal antibody.

© 2022 The Authors. Publishing services by Elsevier B.V. on behalf of KeAi Communications Co., Ltd. This is an open access article under the CC BY-NC-ND license (<http://creativecommons.org/licenses/by-nc-nd/4.0/>).

Introduction

The rapid expansion of available genetic data greatly contributes to identifying the genetic roots of many diseases, such as cancers, virus infections, Parkinson's disease, Alzheimer's disease and inherited diseases.¹ In order to fulfill the clinical potential of these genetic discoveries, we need to accelerate the development of novel therapeutic strategies that can specifically modulate the expression levels of disease-associated genes in target cells *in vivo*. RNA interference is a conserved biological process for neutralizing targeted messenger RNAs (mRNA). Two types of small RNA molecules, small interfering RNA (siRNA) and microRNA (miRNA), play central roles in RNA interference (RNAi). siRNAs are exogenous RNA duplexes that act primarily as inhibitors of gene transcription. miRNAs are endogenous small non-coding RNAs that act by regulating gene transcription and preventing translation of many different mRNAs.² Accumulating evidence has demonstrated that silencing of disease-associated genes by these RNAi mechanisms offers great therapeutic potential and the ability to act on targets considered "non-druggable" by small molecules and biologics, as they can be designed to affect virtually any gene of interest.^{2–4} However, major challenges such as nuclease degradation, poor intracellular delivery, non-specific cell delivery, rapid renal clearance, and inflammatory responses have limited the clinical application of small RNA-mediated gene silencing strategies.^{5–7}

Although advancement of chemical strategies have been used to significantly improve the clinical potential of RNAi-based therapeutics,^{5–7} the effective delivery of highly charged (polyanion) RNAs into cells across the anionic plasma membrane remains.⁵ Once the small RNA therapeutics are internalized into the cells by endocytosis, they often remain trapped in endosomal vesicles and will be degraded in the lysosomal compartment, which is a current limiting hurdle for the effective intracellular delivery of RNAi-based therapeutics.⁵ To overcome these limitations, a variety of carriers have been proposed for the effective delivery of RNAi therapeutics into cells by their unique characteristics, such as membrane fusion, pore formation, and cell-penetrating peptides.^{7,8} However, still only a limited number of delivery carriers have been approved for clinical use due to their potent cytotoxicity and suboptimal efficacy.^{7,9}

Another challenge for the clinical application of RNAi therapeutics is delivering a therapeutic dose of RNA oligonucleotides to the desired cells and tissues *in vivo*, except the liver where the majority of delivery carriers localize

after systemic administration.¹⁰ Cell-specific delivery could be achieved by attaching targeting molecules that bind to target cell-specific surface receptors. Advancements of aptamer research have demonstrated that DNA or RNA aptamers can bind to specific targets with high affinity due to their stable three-dimensional structures.¹¹ By attaching aptamers to the delivery carriers, the small RNA oligonucleotides in the carriers can be efficiently taken up by receptor-mediated endocytosis and deposited into endosomes.¹⁰ However, a major challenge is how the RNAi oligonucleotides can escape endosomes and gain access to the cytosol to modulate target gene transcription. Here we described a cation-dependent nano-platform that not only has extended half-life and cancer cell-targeting specificity but also allows escape from the endosomal compartment for efficient target silencing. Accordingly, our data have important implications for molecular therapy.

Materials and methods

Animals

Eight-week old BALB/c mice were used for the animal studies. All the mice were maintained in the Research Animal Facility at the Institute of Human Virology, University of Maryland Baltimore. The Institutional Committee on the Use and Care of Animal approved all procedures involving experimental animals.

Aptamer and miRNA chimera preparation

Anti-cKIT DNA aptamer, as described in the previous report,¹² was truncated to generate a shorter sequence, but retained its binding affinity to the cKIT receptor (5'-ATTGGGGCCGGGGCAAGGGGGGGGTACCGTGGTAGGAC-3'). For miR-26a chimera preparation, the cKit-aptamer miR-26a chimera was assembled from three DNA/RNA hybrid sequences by complementary base pairing (Fig. S1). These sequences were (1) 5'-A^{*}T^{*}T^{*}*GGGGCCGGGGCAAGGGGGGGGTACCGTGGTAGGAC/C3 spacer/CCU^{*}AUUCU^{*}G^{*}G-3' for cKit aptamer + passenger sequence 1, (2) 5'-G^{*}U^{*}UACUUGCACG/TEG (triethylene glycol)-cholesterol-3' for RNA passenger sequence 2 + cholesterol, and (3) 5'-U^{*}U^{*}CAAGUAAUCCAGGAUAGG^{*}C^{*}U-3' for miR-26a sequence (RNA sequences were represented as italic). The DNA aptamer was conjugated with the passenger sequence via three carbons spacer (C3 linker), that provides spacial flexibility between the aptamer and double stranded RNA, which would not interrupt binding of the aptamer to its

target. The C3 spacer was further replaced with longer 6-chain polyethylene glycol (PEG_{n = 6}) spacer (Spacer 18) (Integrated DNA Technologies, Coralville, IA, USA) for Light_PEG form. The control miRNA sequence is 5'-**G*G*CUGAUCACGUCGAUAAAU*A*U**-3', that is derived from *Arabidopsis thaliana* with no expected binding mRNA sequences in mouse and human according to NIH blast search. To prevent serum degradation, the pyrimidine bases of the passenger RNA sequences were modified with 2'-fluoro RNA (bold) and some purine bases were modified with 2'-O-methyl RNA (underline). The 5'- or 3'-end of oligonucleotides were modified with phosphorothioate bonds (asterisks). These oligonucleotides were synthesized and purified by RNase-free HPLC at Integrated DNA Technologies or TriLink Biotechnologies (San Diego, CA).

To assemble the chimera molecule, the cKit aptamer + passenger sequence 1 was initially folded into its three-dimensional structure by a short denaturation-renaturation step (95 °C 10 min, 10 min snap-cooling on ice) in duplex buffer (100 mM Potassium Acetate; 30 mM HEPES, pH 7.5) (Integrated DNA Technologies) with 2.5 mM MgCl₂ (Thermo Fisher Scientific, Waltham, MA). Then, the three components were mixed in equal molar ratios and slowly assembled through a temperature-controlled annealing reaction (50 °C 30 min, 37 °C 60 min, and 4 °C; 0.1 °C/s) on a thermal cycler (T-100 thermal cycler, Bio-Rad, Hercules, CA) and stored at -20 °C. To form micelle-like nanoparticles, 6.7 μM of annealed oligonucleotide was incubated with 5 mM MgCl₂ for 1 h at 25 °C. The particles were further sterilized by 0.22 μm filter (Millipore Sigma, Burlington, MA) (Fig. S1).

Critical micelle concentration measurement

Fluorescence spectroscopy was used to estimate the critical micelle concentration (CMC) of the delivery platform using a hydrophobic fluorescent probe following the manufacturer's protocol (CMC-535 detergent assay, G-Bioscience, St. Louis, MO) at 25 °C. The fluorescence intensity of probe versus RNA micelles concentration was measured using a spectrofluorometer (SpectraMax iD3, Molecular Devices, San Jose, CA) with an excitation wavelength of 535 nm and emission wavelength of 485 nm at 25 °C.

Transmission electron microscopy

The delivery platform particles were visualized by transmission electron microscopy using a FEI tecnai T12 at the Electron Microscopy Core Imaging facility in the University of Maryland, Baltimore. The platform was loaded on a copper grid, followed by blotting of excess liquid prior to negative staining with 1% uranyl acetate. The grid was visualized under the electron microscope at 80 kV and magnifications at 21,000 x.

Physicochemical characterization

The particle size and zeta-potential of the delivery platform (6.7 μM) were measured by dynamic light scattering (DLS) using a Nanosizer Nano ZS (Malvern Instruments, UK). All the scattered photons were collected at a 173°-

scattering angle. The scattering intensity data was processed using the instrumental software to obtain the hydrodynamic diameter and the size distribution (400 μL 25 °C). The Zeta potential of the particles was also measured by Zetasizer Nano ZS at 25 °C.

Serum degradation assay

The various forms μM miR-26a chimera (with or without MgCl₂) at 6.7 were incubated with human serum (Sigma Aldrich, St. Louis, MO) at 37 °C for various time periods. These solutions were then mixed with an equal volume of RNase-free water, incubated at 95 °C for 5 min, and centrifuged at 4 °C. A portion of the supernatants were used for qPCR of the miR-26a sequence and quantified with a standard curve of dose-titrated miR-26a chimera.

Real-time PCR

Total RNA from cell lines and mouse tissues were extracted by RNeasy Plus Mini kit (Qiagen, Valencia, CA, USA). *miR-26a* levels were quantified by Taqman microRNA assay (assay ID; 000405) that covered both human *has-miR-26a-5p* and mouse *mmu-miR-26a-5p* (Thermo Fisher Scientific) according to the manufacturer's protocol. Mouse *Ezh2* levels were quantified by Taqman gene expression assays (assay ID: Mn00468464_m1). Mouse *Cxcl9* levels were quantified by Taqman microRNA assay (assay ID; Mm00434946_m1). Mouse *β-actin* (Taqman gene expression assays, assay ID; Mm02619580_g1) was used as an endogenous control. Real-time qPCR was performed on QuantStudio 3 (Thermo Fisher Scientific).

Flow cytometry analysis

Anti-mouse cKit (clone 2B8) APC (Cat# 553356) (BD Biosciences, San Jose, CA), and anti-mouse CD3 antibody (clone 17A2) APC (Cat#100235) (Biolegend, San Diego, CA) were used for flow cytometry. For binding analyses of cKit aptamer-miR-26a chimera, the miR-26a was conjugated with Alexa Fluore (AF) 488-green fluorescent dye (Integrated DNA Technologies). The cKit receptor^{+/-} mouse embryonic fibroblast cell line (MEF) was collected with Accutase cell detachment solution (Biolegend) and incubated with 1 μM miR-26a chimera for 10 min in PBS buffer containing 0.45% glucose, 100 mg/L tRNA, 0.1% BSA, 2.5 mM MgCl₂. For inflammatory cytokine analyses, the levels of IL-6, TNF-α and IFN-γ in peripheral blood were determined by cytometric beads assay kit for mouse inflammation (BD Bioscience). These flow cytometry analyses were performed using FACS Canto II (BD Bioscience) and the data were analyzed by FlowJo software (FLOWJO, Ashland, OR).

Cell culture

No cell lines used in this study were listed in the database of cross-contaminated or misidentified cell lines suggested by International Cell Line Authentication Committee (ICLAC). MEF was purchased from ATCC (Manassas, VA). The MEF cell line was cultured in DMEM medium containing 10% FBS, 2 mM L-Glutamine, and Penicillin/Streptomycin

(Thermo Fisher Scientific). For overexpression of mouse c-Kit in MEF cells, a construct of mouse c-Kit (pUNO1-mKIT, InvivoGen, San Diego, CA) was transfected by Lipofectamine 3000 (Thermo Fisher Scientific) following by 4 $\mu\text{g}/\text{mL}$ blasticidin selection (InvivoGen). A mouse breast cancer cell line (TUBO) derived from BALB/c mice transgenic for the transforming rat HER2/neu oncogene (BALB-NeuT) were gifted from Dr. Yang-Xin Fu at the University of Texas Southwestern Medical Center. The TUBO cell line was cultured in DMEM medium containing 10% FBS, 2 mM L-Glutamine, and Penicillin/Streptomycin (Thermo Fisher Scientific).

Immunofluorescence staining

c-Kit^{+/+} MEF cells were grown on a chamber slide (Nunc, Lab-Tek Chamber Slide) for 2 days. Alexa Fluor 488-labeled miR-26a chimera (1 μM) was incubated with the cells at 37 °C. After washing with PBS, the cells were fixed with 4% formaldehyde and washed again with PBS. Magic Red substrate (MR-(RR)2, Immunochemistry Technologies, Bloomington, MN) or 10k MW Dextran (AF546) (Thermo Fisher Scientific) was added with miR-26a chimera for 3 h to measure the leakiness of endosomes in live cells according to the manufacturer's protocol. The fixed cells were mounted with Prolong Gold antifade reagent containing DAPI (Thermo Fisher Scientific). The cells were then visualized by fluorescence microscope (Olympus BX51) (Olympus, Center Valley, PA).

Magnesium measurement

After treatment of 6.7 μM miR-26a chimera under various acidic pH conditions at 25 °C for 1 h, the solution was neutralized with 100 mM Tris-HCl (pH7.5) right before the free magnesium levels in the solution were measured by magnesium assay kit (Abcam, Cambridge, MA) following the manufacturer's protocol. After incubation the absorbance was read on a plate reader (SpectraMaxiD3, Molecular Devices) at 450 nm.

Cell viability and cytotoxicity assay

To assess the cell viability of c-Kit⁺ MEF cells and TUBO cell lines treated with the delivery platform (4000 cells/well in 96 well plate), the culture medium was replaced with 0, 1, 2 and 4 μM of miR-26a chimera-containing medium. After 24 h incubation, 10 μL CCK-8 assay reagent (Cell Counting Kit-8; Dojindo Corporation, Tokyo, Japan) was added to each well. After 2 h at 37 °C, the absorbance at 450 nm was determined using a plate reader (SpectraMaxiD3, Molecular Devices). Negative (vehicle only) and positive (cells treated with 500 μM hydrogen peroxide controls for cell death) were run with each set of experiments. Three replicates were prepared for each sample.

The LDH release assay was performed to assess the cytotoxic potential of the delivery platform. The cultured c-Kit⁺ MEF cells were seeded in a 96-well culture plate in 100 μL of culture media. Three replicates were prepared for

each sample. The supernatant (50 μL) of the cells was transferred to a 96-well plate. After adding the LDH reaction solution (50 μL) (CyQuant LDH Cytotoxicity Assay, Thermo Fisher Scientific) the plate was incubated for 30 min. After incubation the absorbance was read on the plate reader (SpectraMaxiD3, Molecular Devices) at 490 nm and 680 nm.

For calculation of the IC₅₀ for various forms of miR-26a chimera with TUBO cells, the culture medium in 96-well plates was replaced with 1 μM miR-26a chimera containing medium. After 3 days of incubation, 10 μL CCK-8 assay reagent was added to each well. After 2 h, the plates were read on the plate reader (SpectraMaxiD3) at 450 nm. IC₅₀ values were calculated by linear approximation regression of the percentage survival versus the drug concentration using ED50V10 Excel add-in software (ED50Plus v1.0, Instituto Nacional de Enfermedades Respiratorias, Mexico).

Pharmacokinetics study

miR-26a chimera at 0.9 mg/kg was intravenously injected into BALB/c mice ($n = 3$) for various time periods. 25 μL of plasma prepared from peripheral blood in EDTA-treated tubes was immediately mixed with 25 μL of RNase-free water and incubated at 95 °C for 5 min, then centrifuged at 4 °C. The supernatants were used to determine the plasma concentration of miR-26a chimera by RT-qPCR for miR-26a using the standard curve of miR-26a chimera. Pharmacokinetics data analysis was performed using PKSolver software.¹³

Tissue distribution analysis

For the *in vivo* distribution study, 2.4 mg/kg of Alexa Fluor 647-conjugated miR-26a loaded c-Kit-aptamer positive platform (Light_PEG) or c-Kit-aptamer negative platform (No aptamer (+Chol)) was intravenously injected into c-Kit⁺ TUBO tumor-bearing mice. Surface fluorescence from mice tissues (*ex vivo*) harvested 24 h after injection were visualized by *in vivo* fluorescence imager (IVIS) (PerkinElmer, Waltham, MA) set at medium binning, F-stop 1, and auto exposure. *In vivo* surface fluorescence of manually defined regions of interest was quantitated as average radiance efficiency ($[\text{p/s}/\text{cm}^2/\text{sr}]/[\mu\text{W}/\text{cm}^2]$) using Living Image software (PerkinElmer).

In vivo safety assessment

For safety assessment, complete blood counts were measured by Hemavet 950FS (Drew Scientific, Miami Lakes, FL). Serum concentrations of ALT (Alanine aminotransferase) were measured by Randox RX Monza clinical chemistry analyzer (Randox, Kearneysville, WV) according to the manufacturer's instructions. Plasma concentrations of BUN (Blood urea nitrogen) were measured using Urea nitrogen direct (Stanbio, Boerne, TX) by SpectaMAX iD3 (Molecular Devices).

For histochemistry analysis, transversal sections of liver, lung, heart and kidney were fixed with 4% paraformaldehyde, and embedded in paraffin. The tissue

sections were processed and stained using Harris's H&E (Sigma–Aldrich). Images of each tissue section were captured by BX51 digital light microscope (Olympus).

***In vivo* tumor inhibition studies**

For breast cancer models, the female BALB/c mice were subcutaneously injected with 2×10^6 viable TUBO cells in their right hind limbs. After the tumor grew to 5 mm in diameter, mice were randomly divided into groups for treatment with either the vehicle control (100 μ l the duplex buffer), or with 2.4 mg/kg miR-26a chimera or control chimera intravenously injected through their tail veins. During the treatment period, 100 μ g of anti-mouse Ctl4 antibody (clone 9D9, BioXcell, Lebanon, NH) were intraperitoneally injected into the mice on day 3. Tumor sizes were measured in two dimensions every 3 days. Tumor volume (V) was calculated as: $V = (1/2) S^2 \times L$ (S, the shortest dimension; L, the longest dimension). Plasma concentrations of Cxcl9 were measured by mouse Cxcl9 DuoSet ELISA (R&D systems, Minneapolis, MN). The concentrations of Cxcl9 in tumors were measured by the Cxcl9 DuoSet using the supernatant of minced tumors (0.2 g). For T cell infiltration analysis, fresh tumor tissues were dissociated by manual mincing followed by incubation in RPMI-1640 medium with collagenase and hyaluronidase (Stem Cell Technologies, Cambridge, MA) for 20 min at 37 °C. After dissociation, cell suspensions were filtered with a 100 μ m cell strainers and used for flow cytometry analyses.

Statistics

Data were analyzed using a Student's *t* test to compare between two groups, and two-way repeated-measures ANOVA, followed by the Bonferroni post-hoc procedure for follow-up pairwise comparison. Survival data were analyzed by a Kaplan–Meier survival analysis with log-rank test. Statistical calculations were performed using GraphPad Prism software (GraphPad Software, San Diego, CA). All data were presented as mean \pm standard deviation. Asterisks denote the significant differences. **P* < 0.05, ***P* < 0.01.

Results

Magnesium induces assembling of nano particles for small RNA delivery

We previously demonstrated that our delivery platform could deliver a small RNA oligonucleotide (miR-26a) to target cells and silence its target genes, including *Ezh2* and *Bak1*, *in vitro* and *in vivo*.¹⁴ This platform comprises (1) a guide strand RNA sequence (22 nt), (2) a first RNA passenger strand sequence (10 nt) linked with a cell surface receptor-targeting DNA aptamer via a three carbon linker, and (3) a second RNA passenger strand sequence (12 nt) conjugated to cholesterol via a triethylene glycol (TEG) spacer (Fig. S1). These three components were mixed in equal molar ratios and form a double strand RNA oligonucleotide by temperature-controlled annealing according to

the complementary base pairing of the nucleic acid sequences (Fig. S2). As our platform contains hydrophobic cholesterol covalently linked to the 3' of the annealed of hydrophilic oligonucleotides (Fig. S1), it creates an amphiphilic structure with the potential to form micelle-like particles with a hydrophobic cholesterol core surrounded by a hydrophilic oligonucleotide shell.¹⁵

However, the negative charge of the oligonucleotides may limit self-assembling.¹⁶ To overcome this limitation, we added a grading concentration of magnesium chloride to the oligonucleotide-cholesterol formulation and evaluated micelle formation using a fluorescence dye (CMC-535) that emits a fluorescent signal upon interaction with hydrophobicity in aqueous solutions. As shown in Figure 1A, a drastic increase of fluorescence intensity was observed when 1 mM of magnesium chloride was added, which indicated a major increase in micelle-like particle formation. The increase was dose-dependent and plateaued when 5 mM of magnesium was added. The critical micelle concentration (CMC) of this particle was 3×10^{-7} M (Fig. 1B), which represents a value 40 times more stable than Polysorbate 80 (CMC = 1.2×10^{-5} M) that is widely used for micellar drug formulation.¹⁷ To evaluate the particle structure, we visualized it by transmission electron microscopy and observed spherical objects 20–40 nm in size (Fig. 1C). Dynamic light scattering analysis demonstrated a peak particle diameter of 30 nm with almost neutral net charge of particle boundary (zeta-potential = -0.086 mV) (Fig. 1D). Of note, we did not observe any major particle structures in the absence of magnesium, confirming that magnesium is required for particle formation. Notably, we did not observe any aggregates even with a high concentration of delivery platform (33 μ M, turbidity <0.05 at 490 nm). Interestingly, this magnesium-induced particle structure significantly inhibited the susceptibility of loaded-small RNA oligonucleotide (miR-26a) to serum nuclease degradation compared to the delivery platform without magnesium (Fig. 1E; Fig. S3A).

To determine the functional delivery of the miR-26a by our targeted delivery platform, we treated c-Kit⁺ TUBO breast cancer cells with a c-Kit-targeting miR-26a-loaded delivery platform (miR-26a chimera) formulated with or without magnesium chloride (Fig. 1F; Fig. S3A). Based on the expression of *Ezh2*, a validated miR-26a target gene, magnesium-induced nanoparticles provided the most effective platform in silencing *Ezh2* expression.

pH-dependent magnesium release, nanoparticle disassembly and lysosomal leakage

We have recently reported the target specificity of our delivery platform to cancer cells and hematopoietic progenitor cells using a c-Kit aptamer.¹⁴ To determine whether the magnesium-induced nanoparticles still retain the specificity, we conjugated the AF 488-green fluorescent dye to miR-26a, assembled the nanoparticles with the fluorescent miR-26a in the presence of magnesium, and incubated the nanoparticles with mouse c-Kit-positive or negative MEF cells *in vitro* (Fig. 2A). Flow cytometry analysis demonstrated that the magnesium-induced nanoparticles bound to the c-Kit⁺ MEF cells but barely to the c-Kit⁻ cells (Fig. 2A). To evaluate the

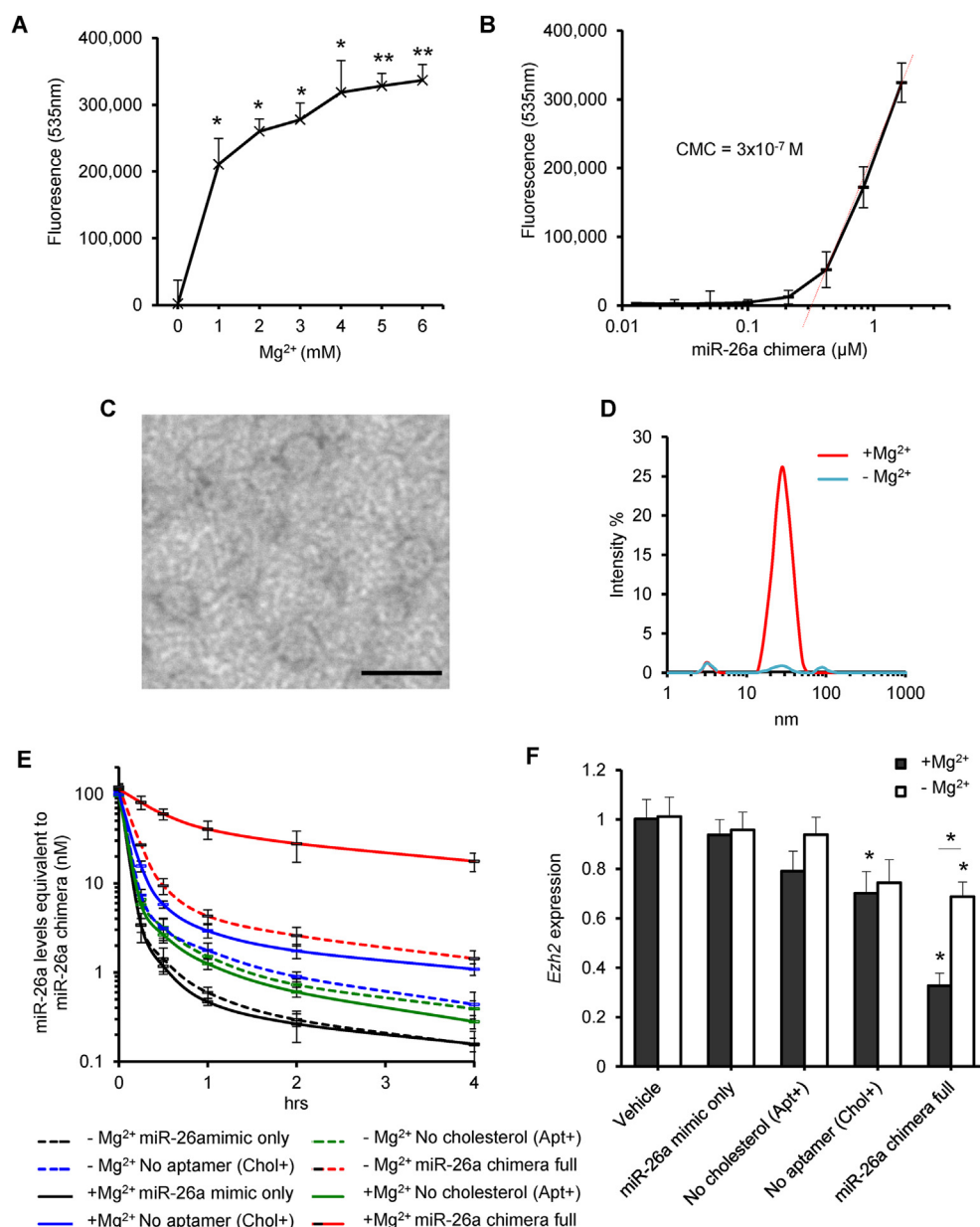


Figure 1 Magnesium induced assembly of nanoparticles with improved resistance to degradation and miRNA function. **(A)** Micelle formation under various concentrations of MgCl_2 detected by hydrophobic-incorporation of fluorescent dye (CMC-535). **(B)** Plots of fluorescence intensity at 535 nm under various concentrations of the delivery platform. The critical micelle concentration (CMC) was 3×10^{-7} M. **(C)** Transmission electron microscopy image of the delivery platform nanoparticles using negative staining. Scale bar, 50 nm. Representative image of a single experiment. **(D)** The particle size distribution of the delivery platform with MgCl_2 (+ Mg^{2+}) or without MgCl_2 (- Mg^{2+}) measured by dynamic light scattering. Representative image of two independent experiments. **(E)** Stability of each component of the miR-26a delivery platform against serum degradation *in vitro*. The miR-26a chimera of particle form (+ Mg^{2+}) or non-particle monomer form (- Mg^{2+}) in various formats (Fig. S3A) was incubated with human serum for various time periods. Stability was measured by qPCR for miR-26a. **(F)** Functional effect of each moiety in the delivery platform for gene silencing by miR-26a. The c-Kit-targeting miR-26a chimera (1 μM) in various formats (Fig. S3A) with or without MgCl_2 were incubated with c-Kit + TUBO cancer cells for 2 days. The expression levels of a miR-26a target gene, *Ezh2*, were measured by qPCR. Asterisks denote the significant difference compared to vehicle controls. (A, B, E, F) Data shown as mean \pm SD of combined data from two independent experiments, each with duplicated samples. * $P < 0.05$, ** $P < 0.01$.

fate of nanoparticles after binding to c-Kit, we visualized the cellular distribution of the AF488-conjugated miR-26a in the c-Kit⁺ MEF cells using fluorescence microscopy. As shown in Figure 2B, we observed a punctuated intracellular

distribution of the loaded-miR-26a after 30 min of treatment, which suggest endocytosis of the miRNA. After 2 h, the miR-26a diffused throughout the cells, which suggest that the miRNA has escaped the endocytic compartments. Since

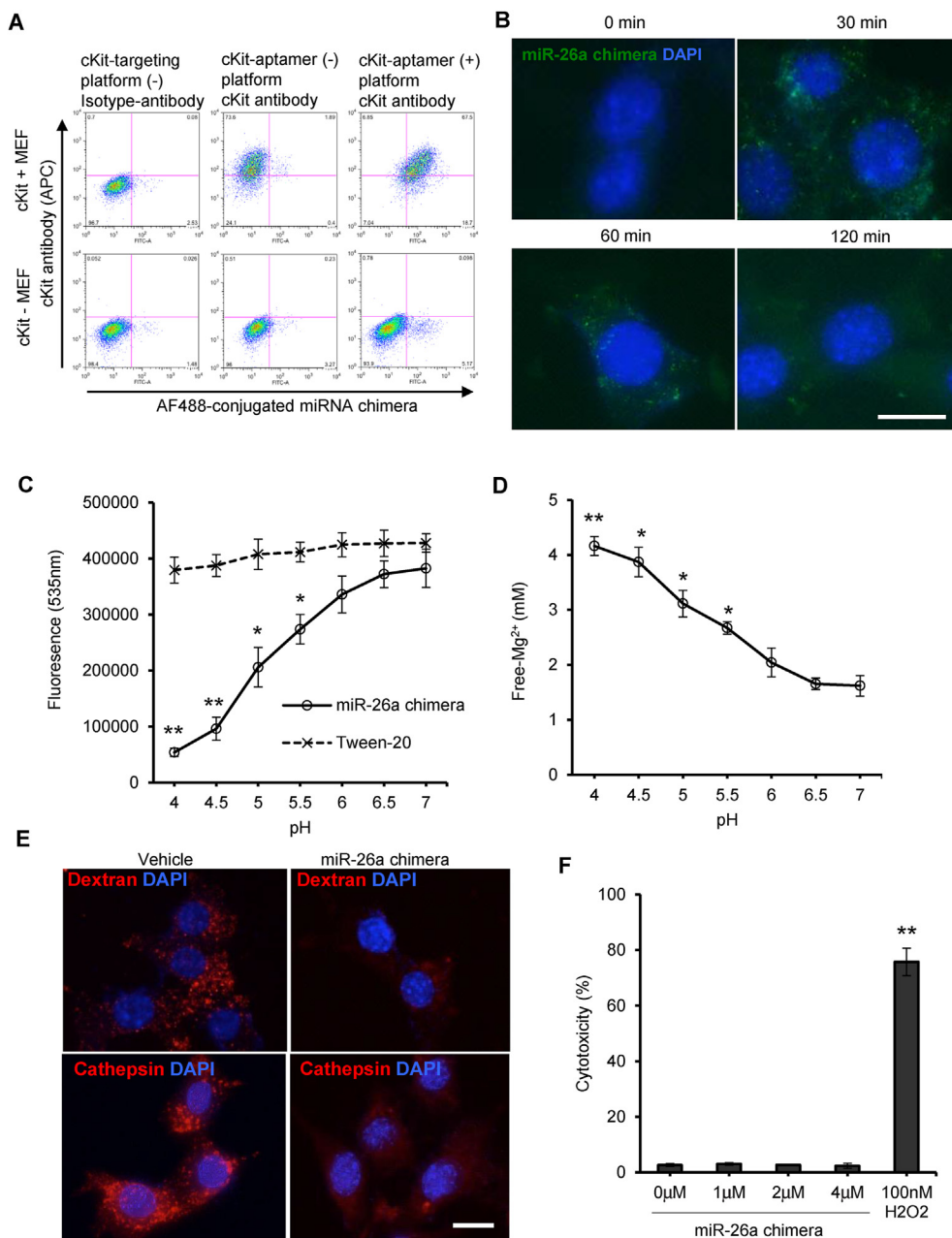


Figure 2 The pH-sensitive delivery platform induced endosomal leakage but not cytotoxicity. **(A)** Target specificity of the c-Kit-targeting delivery platform linked with anti-c-Kit DNA aptamer. The c-Kit-targeting aptamer-positive platform bound specifically to c-Kit⁺ MEF cells *in vitro*. **(B)** Visualizing uptake of c-Kit-targeting miR-26a chimera in c-Kit⁺ MEF cells over 120 min. The AF488-conjugated miR-26a chimera (Green) was incubated with the cells at 37 °C. After washing with PBS, the cells were fixed with 4% formaldehyde and images were acquired on a fluorescent microscope. Scale bar, 5 μm. **(C)** Destabilization of micelle particles of the miR-26a chimera under acidic pH conditions detected by hydrophobic-incorporation of fluorescent dye (CMC-535). Tween-20 is used as a control. Asterisks denote significant differences compared to pH 7.0. **(D)** Free magnesium concentration in solution of the delivery platform nanoparticles incubated under various pH conditions for 1 h. Asterisks denote significant differences compared to pH 7.0. **(E)** Release of an endosomal trafficking fluorescent probe (10 k Dextran, red) from endosomes in c-Kit⁺ MEF cells at 3 h after treatment with vehicle or miR-26a chimera (Top panels). Release of another fluorescent probe (Cathepsin enzymatic fluorescent substrate, Magic Red) from endosomes in c-Kit⁺ MEF cells at 3 h after treatment with vehicle or miR-26a chimera (Bottom panels). Scale bar, 5 μm. **(F)** Lack of cytotoxicity of miR-26a chimera to cKit⁺ MEF cells treated with various concentration of miR-26a chimera for 24 h as detected by LDH release assay. Asterisks denote the significant difference compared to 0 μM of miR-26a chimera treatment. (A, B, E) Representative images of two independent experiments. (C, D, F) Data shown as mean ± SD of combined data from two independent experiments, each with duplicated samples. **P* < 0.05, ***P* < 0.01.

endocytic compartments undergo progressive acidification, we tested the fate of nanoparticles under different pH conditions. Using the micelle-encapsulated fluorescence probe, we evaluated micelle stability under pH that range from extracellular pH (7.0) to those found in the lysosome (4.5–5.0). As shown in Figure 2C, the micelles formed by the miRNA nanoparticle were progressively disrupted at pH that resembles late endosome or lysosome (pH 5.5–4.0), which suggests that the magnesium-induced nanoparticles would likely disassemble as they traffic through the endocytic-lysosomal compartment. To understand the mechanism, we evaluated if the magnesium is released under acidic conditions. As shown in Figure 2D, progressive lowering of pH led to a progressive increase of free magnesium. Since nanoparticle formation depends on magnesium, the magnesium release is consistent the nanoparticle disassembly in Figure 2C.

Disassembly of the nanoparticles exposes cholesterol that may destabilize the endocytic compartment,¹⁸ with the release of magnesium ions potentially building magnesium salts in the endocytic compartment due to osmotic imbalance.¹⁹ Using AF647-conjugated 10k MW dextran that is used for visualizing the endocytic compartment, vehicle treated control cells that have received fluorescent dextran probe show accumulation of dextran in intracellular vesicles as shown in Figure 2E. In contrast, the cells that received the miRNA chimera nanoparticles showed no such accumulation. These data suggest disruption/leakiness of the endocytic compartment. Since exposure of cholesterol and release of magnesium was most prominent at lysosomal pH, we hypothesize that lysosomes are likely destabilized by the disassembly of miRNA chimera nanoparticles. To test this hypothesis, we treated the cells with a substrate that fluoresces red upon cleavage by active cathepsin enzymes, which is a well-known marker for lysosomes.²⁰ While we observed the punctuated distribution of cathepsin substrate in the c-Kit⁺ MEF cells treated with vehicle, miR-26a chimera treatment abrogated the lysosomal compartment. To test if the lysosomal disruption/leakiness causes non-specific cell death, we examined the cell viability and cytotoxicity using the c-Kit⁺ MEF cells treated with miR-26a chimera nanoparticles. The miR-26a chimera treatment affected neither cell viability (Fig. S4) nor cytotoxicity (Fig. 2F).

Chemical modifications of the oligonucleotides enhance gene silencing, *in vivo* stability, and reduce systemic inflammatory responses to the nanoparticles

Nuclease-mediated degradation reduces half-life of RNAi molecules *in vivo*.²¹ To define the best chemical modifications for our delivery platform,¹⁴ we modified the RNA oligonucleotides with 2'-fluoro pyrimidines, 2'-O-methyl purines and phosphorothioate bonds to confer resistance to RNase (Fig. S3B–D). We found that while modifications at the 5' and 3' ends of the guide RNA (light mimic) allow the molecule to remain active in gene silencing, those with further modifications in the center region of the guide RNA sequence (heavy mimic) significantly interrupted the gene silencing effect of miR-26a with our delivery platform (Fig. 3A). We also observed interruption of the gene silencing

effect by further modifications on passenger RNA sequences with 2'-O-methyl purines (heavy 5'pass and 3'pass) (Fig. 3A, S3B, C). The growth inhibition of various forms of the miR-26a chimera assembled into nanoparticles were assessed using c-Kit⁺ TUBO cancer cells, which demonstrated the IC₅₀ of light mimic form was 3.4-times lower than the heavy mimic form (Fig. 3B; Fig. S5A). These results indicated that the modifications on the guide RNA sequence with 2'-fluoro pyrimidines, 2'-O-methyl purines, and phosphorothioate bonds at the 5' and/or 3' ends, in combination with the passenger sequences with 2'-fluoro pyrimidines and phosphorothioate bonds at the 5' and/or 3' ends (light mimic), were suitable form for our delivery platform (Fig. S3D).

Polyethylene glycol (PEG) is widely used in drug delivery to provide “stealth” properties to the delivery particle surface, which diminished the recognition or uptake by macrophages.²² Replacement of the C3 linker to a low molecular weight PEGn = 6 linker in the light mimic (Light_PEG) did not affect its potent gene silencing effect or growth inhibition activity (Fig. 3A, B; Fig. S3D, S5A, S5A).

We evaluated the pharmacokinetics of the various forms of miR-26a chimera in BALB/c mice and found that both light and heavy modifications significantly improved their half-life compared to other modifications on the guide RNA sequence (Fig. 3C; Fig. S3D, S5B). Conjugation of the light mimic to PEGn = 6 resulted in an extension of half-life. The PEG conjugation also resulted in most significantly reduced inflammatory response (Fig. 3D; Fig. S3D).

The safety assessments of the targeting delivery platform *in vivo*

We performed safety assessments using BALB/c mice treated with the dose-titrated delivery platform (light_PEG form of the miR-26a chimera). Complete blood count (white blood cells, red blood cells, and platelets), liver enzyme (alanine aminotransferase, ALT), and blood urea nitrogen (BUN) levels were unaffected at day 10 after intravenous administration with the miRNA nanoparticle (Fig. 4A–C). miRNA nanoparticles did not cause weight changes when compared to the vehicle control (Fig. 4D). Histopathology analysis with hematoxylin-eosin stain sections of liver, kidney, heart and spleen revealed no abnormalities (Fig. 4E). These results demonstrated the overall safety over extended period of our light_PEG form miR-26a chimera nanoparticle.

miRNA nanoparticles with potent therapeutic effect against breast cancer

To further examine the *in vivo* targeting ability of the delivery platform, the c-Kit targeting platform with AF647-conjugated miR-26a (light_PEG form miR-26a chimera) was injected intravenously into tumor-bearing BALB/c mice with the c-Kit⁺ TUBO breast cancer cells. We observed a significant accumulation of the c-Kit-aptamer positive platform nanoparticles into the c-Kit⁺ tumors (4-fold higher accumulation), instead of liver accumulation (3-fold less accumulation), compared to c-Kit-aptamer negative platform by *in vivo* imaging, indicating that the DNA aptamer on our targeting delivery platform enabled >12-

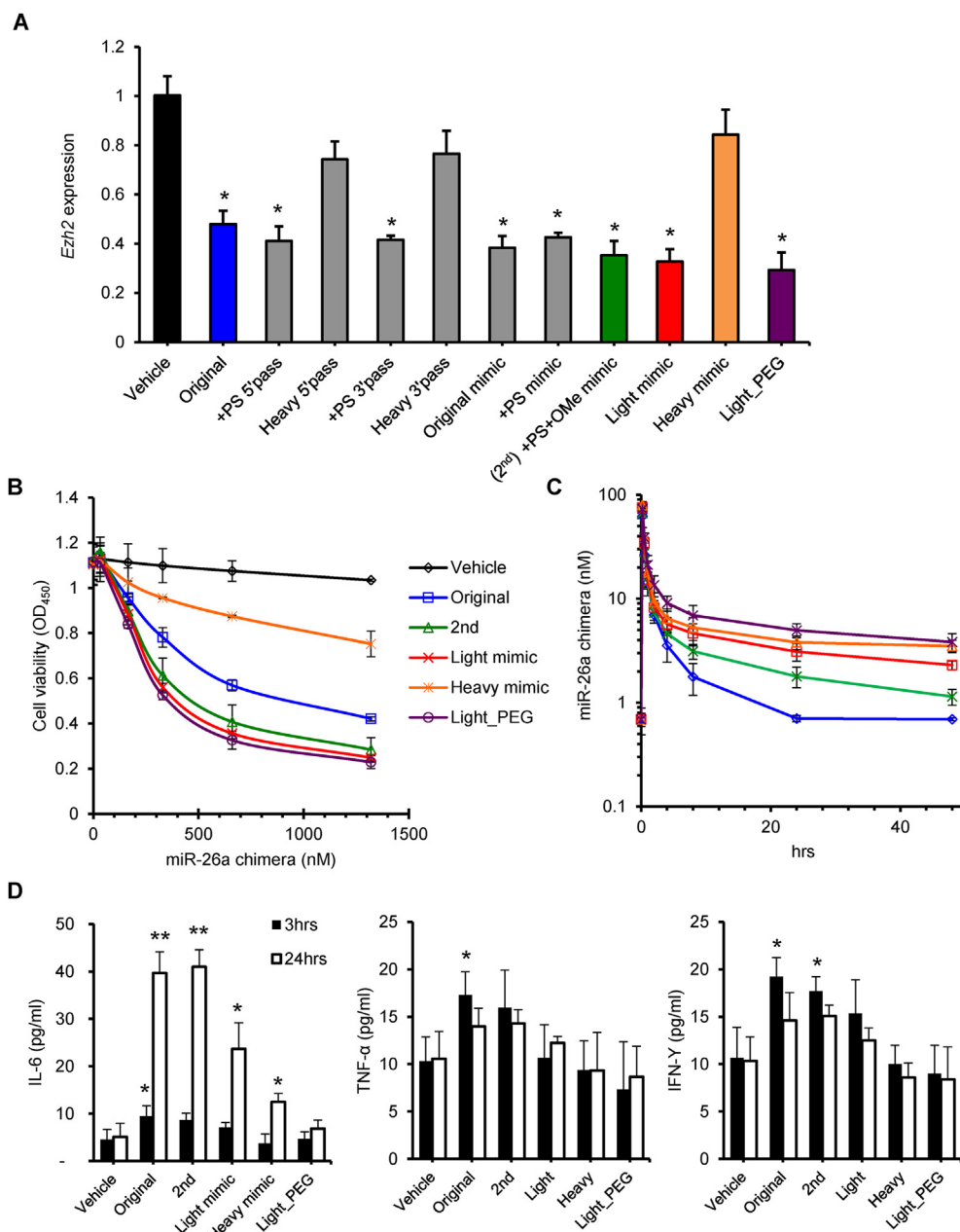


Figure 3 Optimization of chemical modifications on a miRNA delivery platform *in vitro*. (A) The effect of various chemical modifications on the miRNA delivery platform (miR-26a chimera) (see also Fig. S3B–D). The gene silencing effect of different chemical modifications on the miR-26a chimera was determined by qPCR of a miR-26a target gene, *Ezh2*, using c-Kit⁺ TUBO cancer cells treated for 2 days. Asterisks denote the significant difference compared to vehicle treatment. (B) The inhibition of tumor growth by various miR-26a chimera compositions. The TUBO cells were cultured with miR-26a chimeras (1 μM each) for 3 days and the cell viability was measured by CCK-8 assay. (C) Plasma concentration of various forms of the miR-26a chimera. Each miR-26a chimera (0.9 mg/kg) was intravenously injected into BALB/c mice ($n = 3$) for various time periods and plasma concentrations were determined by qPCR for miR-26a. (D) Inflammatory responses against various forms of miR-26a chimera detected by cytometric beads assay for IL-6, TNF- α , IFN- γ in plasma collected at 3 h and 24 h after intravenous administration of 0.9 mg/kg miR-26a chimera into BALB/c mice ($n = 3$). Asterisks denote the significant difference compared to vehicle treatment. (A, B) Data shown as mean \pm SD of combined data from two independent experiments, each with duplicate samples. (C, D) Data shown as mean \pm standard deviation of triplicate and are representative of two independent experiments. * $P < 0.05$, ** $P < 0.01$.

fold higher targeting ability to the target tissue *in vivo* compared to the non-targeting platform (Fig. 5A). Notably, the aptamer also significantly reduced non-specific kidney accumulation of the delivery platform, further supporting

the target specificity of our aptamer-based delivery platform. To evaluate the therapeutic potential of our delivery platform *in vivo*, we treated the c-Kit⁺ breast cancer-bearing BALB/c mice with the miR-26a chimera (light_PEG

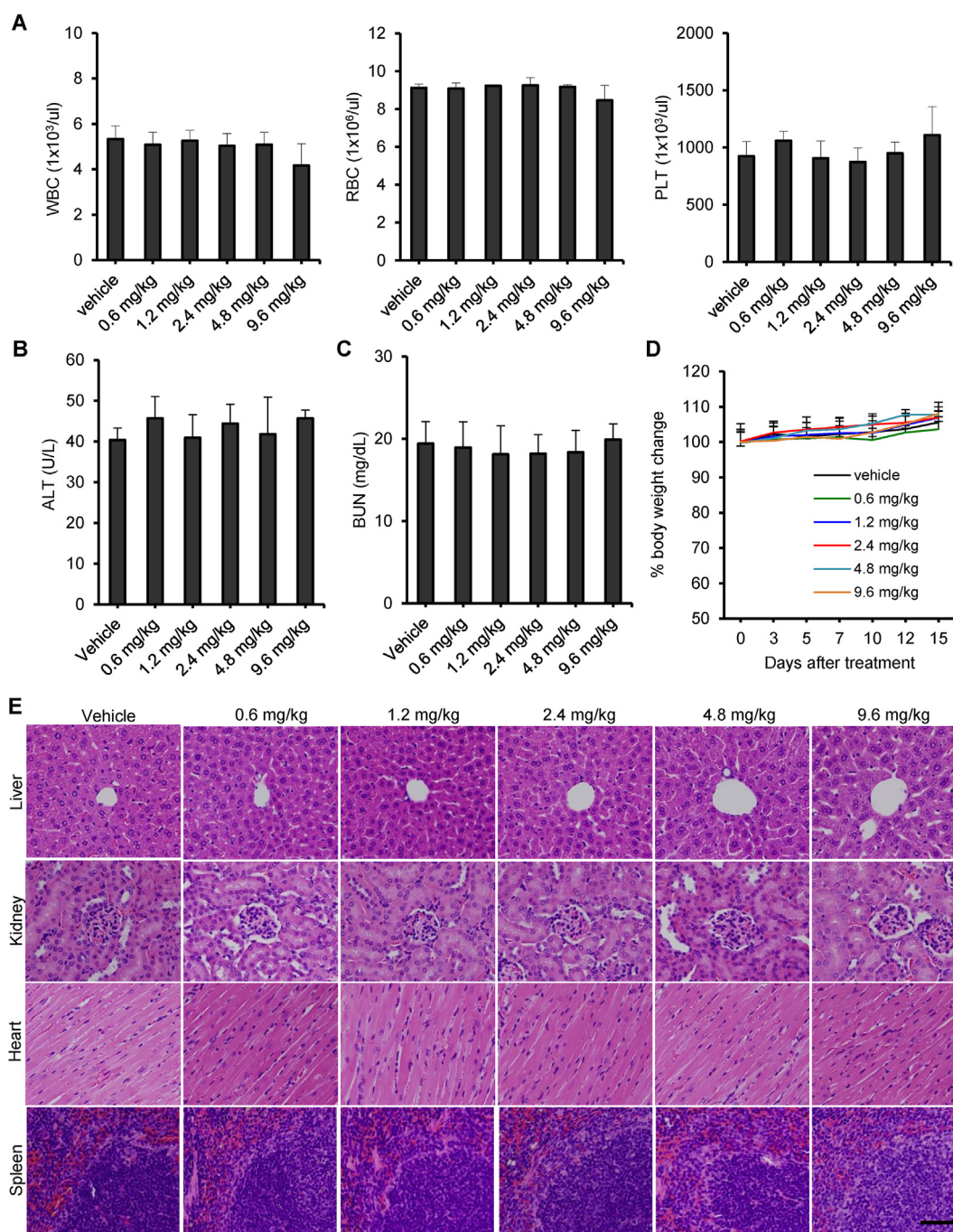


Figure 4 Safety of the most effective miR-26a chimera in mice. **(A)** The numbers of white blood cells (WBC), red blood cells (RBC), and platelets (PLT) in peripheral blood collected at day 10 from BALB/c mice intravenously treated with various doses of optimal miR-26a chimera ($n = 3$). **(B)** The hepatic parameter of ALT in plasma collected at day 10 from the BALB/c mice treated with various doses of miR-26a chimera. **(C)** The nephrotoxic parameter (BUN) in plasma collected at 10 days after the miR-26a chimera treatment. **(D)** Body weight change over time after various doses of miR-26a chimera treatment. There were no significant differences among the various doses of miR-26a chimera treatments in the figures. Data shown are mean \pm standard deviation of triplicate samples and are representative of two independent experiments. * $P < 0.05$, ** $P < 0.01$. **(E)** Histological sections (H&E stain) of liver, kidney, heart and spleen harvested at day 15 after the miR-26a chimera treatment. Scale bar, 100 μm . Representative images of the two independent experiments.

form miR-26a chimera). We observed significant silencing of a validated miR-26a target gene, *Ezh2*, in tumors for at least 3 days after a single intravenous administration of miR-26a chimera (Fig. 5B).

Ezh2 is a histone methyltransferase that is known to suppress expression of a chemokine, *Cxcl9*, in tumors,²³ suggesting that *Cxcl9* is a potential biomarker for effective *Ezh2* silencing *in vivo* by miR-26a chimera treatment.

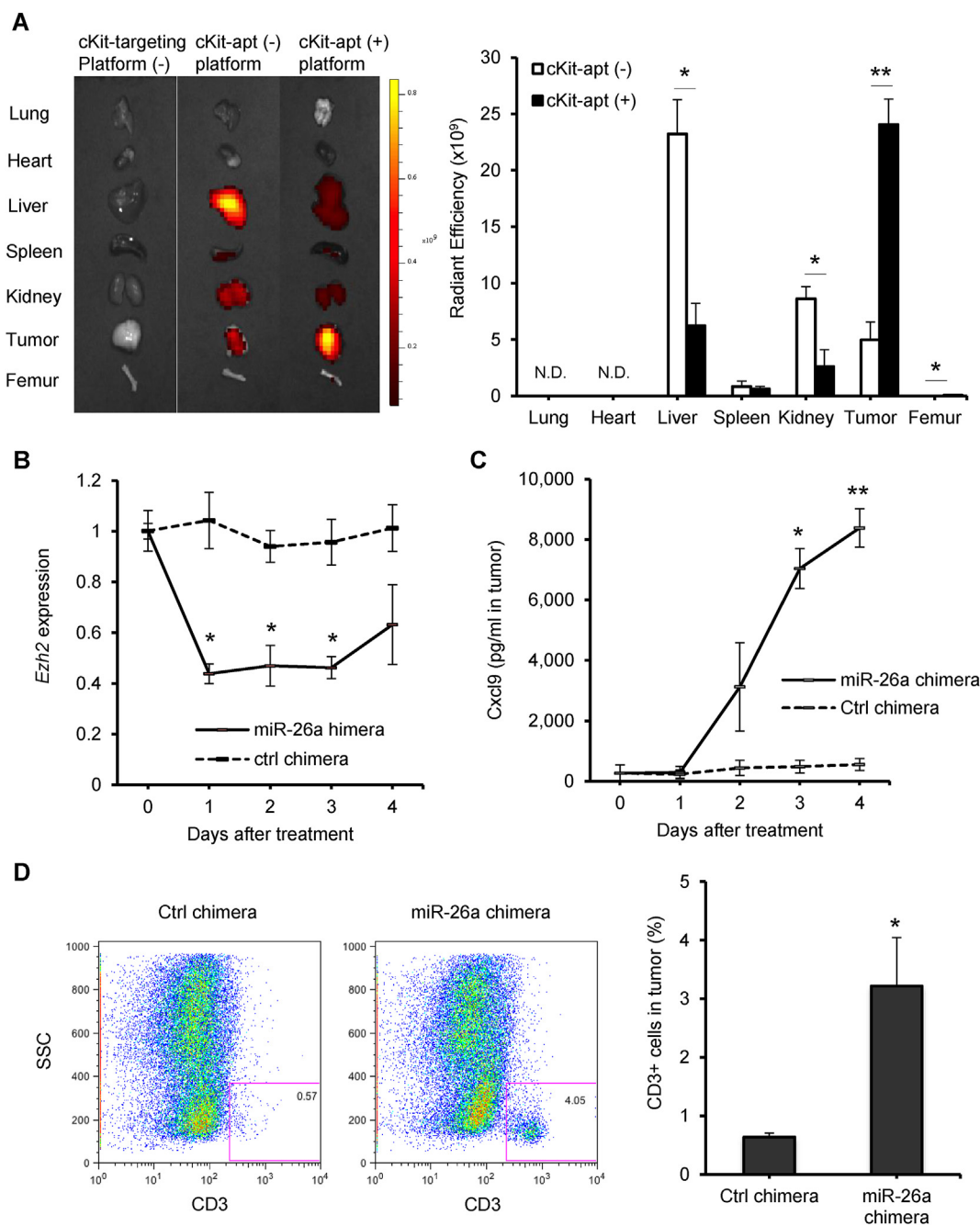


Figure 5 Optimal miR-26a chimera increased T cell infiltration into tumors. **(A)** Tissue distribution of targeting the delivery platform in tumor bearing mice. (Left) The organ accumulations of AF647-conjugated c-Kit-aptamer positive or negative platform (2.4 mg/kg) at 24 h after intravenous injection into c-Kit⁺ TUBO tumor-bearing mice. The images are representative of those from 3 mice per group. (Right) The quantification of organ accumulation between the c-Kit-aptamer negative and positive platforms ($n = 3$). Asterisks denote the significant different between Kit-aptamer negative and positive platforms. N.D. = not detected. **(B)** Gene silencing effect of the miR-26a chimera in the tumors various days after intravenous injection with 2.4 mg/kg of miR-26a chimera into c-Kit⁺ TUBO tumor-bearing mice was determined by qPCR for the miR-26a target gene, *Ezh2* ($n = 3$). Asterisks denote significant difference compared to control chimera treatment. **(C)** Cxcl9 expression in the tumors after miR-26a chimera treatment detected by ELISA using the supernatant of minced tumors ($n = 3$). Asterisks denote significance different compared to control chimera treatment. **(D)** The miR-26a chimera treatment increased CD3⁺ cells in the tumors harvested at day 4. (Left) Representative data of flow cytometry analysis. (Right) Statistics of CD3⁺ T cell infiltration (% among CD45⁺ cells) in the tumors after the miR-26a chimera treatment ($n = 3$). Asterisks denote significant difference compared to control chimera treatment. (B–D) Data shown as mean \pm SD of triplicate samples and are representative of two independent experiments. * $P < 0.05$, ** $P < 0.01$.

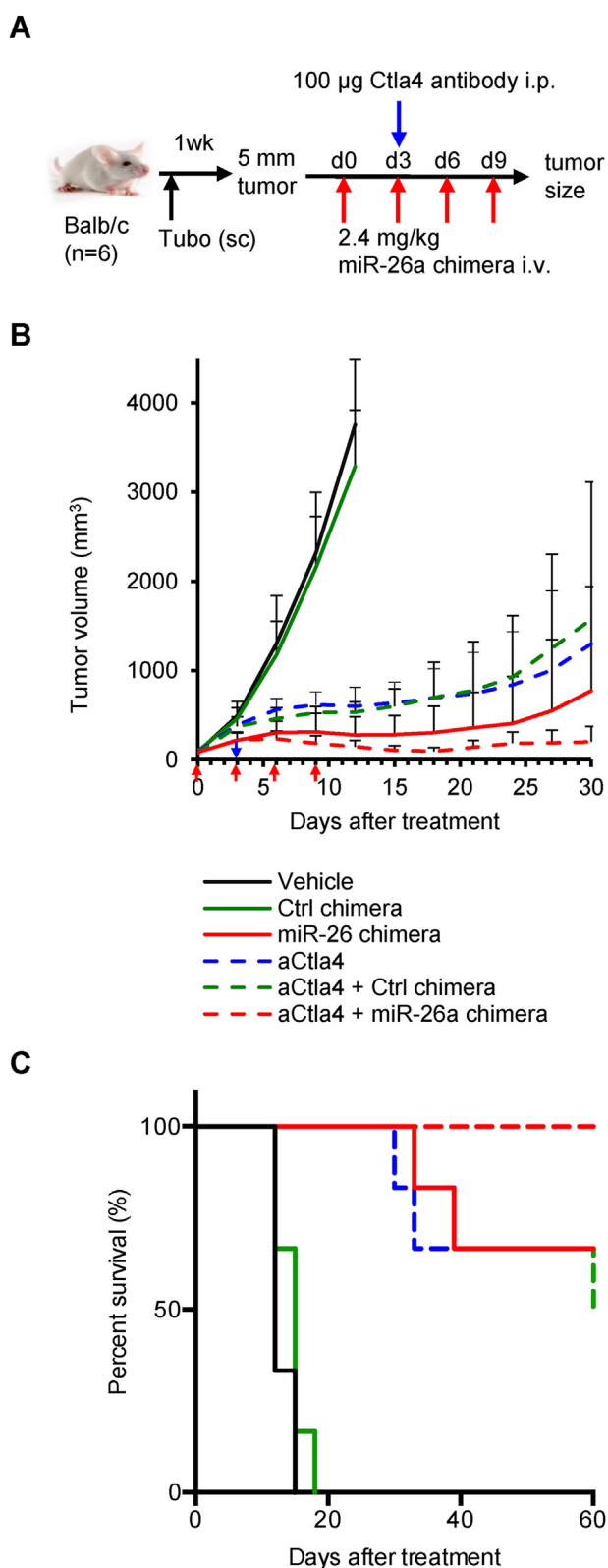


Figure 6 Optimal miR-26a chimera inhibited the growth of breast cancer and increased mouse survival. **(A)** Treatment regimen with miR-26a chimera and anti-Ctla4 antibody (aCtla4). **(B)** Tumor volume over time. The c-Kit⁺ TUBO tumor-bearing mice were treated with 2.4 mg/kg miR-26a chimera (red allows) and/or 100 µg anti-Ctla4 antibody (blue arrow) ($n = 6$). There

Consistent with this notion, we observed significant elevation of Cxcl9 in the tumors and peripheral blood after miR-26a chimera treatment (Fig. 5C; Fig. S6). Since Cxcl9 is an essential chemokine for T cell infiltration into tumor sites,²⁴ we tested whether the elevation of Cxcl9 correlated with T cell infiltration into tumor sites. As shown in Figure 5D, we observed a significant increase of CD3⁺ T cells in the tumors at 4 days after miR-26a chimera treatment compared to control chimera treatment. Since the T cell infiltration in tumor sites is an essential factor for successful immunotherapy with immune checkpoint inhibitors, the increase of T cells in tumors prompted us to test the potential of miR-26a chimera in improving the immunotherapeutic effect. We treated the c-Kit⁺ tumor-bearing BALB/c mice with miR-26a chimera and/or anti-Ctla4 antibody (Fig. 6A). While both miR-26a chimera and anti-Ctla4 antibody monotherapy demonstrated significant inhibition of tumor growth compared to vehicle treatment, their combination dramatically shrunk the tumor sizes at day 9 after the first treatment (or 16 days after tumor cell transplantation) with miR-26a chimera (Fig. 6B; Fig. S7), and extended overall survival (Fig. 6C).

Discussion

We developed a targeted small RNA delivery platform based on magnesium-induced assembly of nanoparticles with a cholesterol core, RNA oligonucleotide shell, and DNA aptamer flare. The platform allows delivery of a large bolus of small RNA therapeutics into a single cell. The size of particle (30 nm) is large enough to avoid renal clearance (less than 5 nm) but small enough to penetrate to target tissues.^{25,26}

Recent advancement of chemical modifications to oligonucleotides significantly improves the pharmacokinetic properties of RNA therapeutics by reducing the susceptibility to nuclease degradation.^{27,28} In our platform, modifications on the 5'- and/or 3'-ends of the guide RNA sequence with 2'-fluoro-pyrimidines, 2'-O-methyl-purines or phosphorothioate bonds, instead of full modifications on center region of oligonucleotide, significantly improved *in vivo* stability while retaining the miRNA function of miR-26a. Of note, we used 2'-fluoro-RNA modifications in our platform for the most of part, which would further stabilize the particle structure due to its higher hydrophobicity, and increase of melting temperature compared to unmodified RNAs or 2'-O-methyl-RNA modifications.^{29,30} Phosphorothioate bonds are known to induce non-specific binding to

was a significant difference at day 3 in ctrl chimera vs. miR-26a chimera ($P = 0.012$), but not between vehicle vs. aCtla4 ($P = 0.066$). At day 6 there were significant differences in vehicle vs. aCtla4 ($P = 0.0011$), and vehicle vs. combination of aCtla4 + miR-26a chimera ($P < 0.0001$). **(C)** Kaplan–Meier survival curve ($n = 6$). There were significant differences in ctrl chimera vs. miR-26a chimera ($P < 0.0006$), vehicle vs. aCtla4 ($P < 0.0006$), ctrl chimera vs. combination of aCtla4 and miR-26a chimera ($P < 0.0006$). Data shown as mean \pm SD of combined data from two independent experiments, each with 3 mice per group.

cell surface receptors for intracellular delivery.³¹ To retain the targeting specificity of the aptamer on our delivery platform, we used a minimum number of phosphorothioate bonds and only at the 5'- and 3'-ends of oligonucleotides. Additionally, magnesium-induced particle structure significantly inhibited the serum degradation of loaded-miRNA.

One of the challenges for the clinical application of RNA-based therapeutics is the unfavorable activation of the innate immune system.³² Our data in Figure 3 and S3 demonstrated that the chemical modifications and replacement of the 3 carbon linker to a longer 6 chain PEG linker significantly reduced inflammatory responses *in vivo*. The PEG linker not only improves *in vivo* stability of micelle particles by its hydrophilicity, but also diminished immune responses against our delivery platform *in vivo*, leading to longer circulation time and reduction of administrative dose and frequency.²²

The effective delivery of RNA-based therapeutics depends on the expression levels of target receptors and the activity of receptor internalization.¹⁰ Like other tyrosine kinase receptors, the c-Kit receptor is known to be over-expressed on cancer cells compared to normal cells, and also rapidly internalized (1.5×10^{-3} /s) in the first 15 min after interaction with its ligands.³³ The target-specific binding and effective delivery of loaded-miRNAs into the cytosol indicate that the c-Kit receptor is an ideal delivery target for small RNA therapeutics to cancer cells. However, the c-Kit receptor is also known to be expressed in normal cells, including hematopoietic stem cells.³⁴ Since we previously demonstrated a therapeutic advantage of a c-Kit-targeting miR-26a chimera for protecting hematopoietic stem cells from chemotherapy-induced apoptosis by silencing a pro-apoptotic gene, *Bak1*, with no apparent adverse effects on hematopoiesis,¹² at the highest doses tested, the targeting strategy using c-Kit receptors to deliver miR-26a to c-Kit⁺ cancer tissue deserves further evaluation.

For maximizing the amount of RNA therapeutics getting into the target cells while minimizing the administrative doses and off-target toxicities, several targeting probes have been investigated, such as glycol-conjugates targeting the asialoglycoprotein receptor (ASGPR), antibodies and aptamers. The ASGPR-based delivery system is a clinically approved probe for effective and selective delivery of siRNA therapeutics to hepatocytes.³⁵ For targeting to other tissues, monoclonal antibodies are proposed as potential targeting probes. However, there are still challenging hurdles for the clinical application, such as antibody-small RNA conjugates forming multimeric aggregates rather than defined molecular species and the difficulty of penetrating tissues due to the large size of conjugates.^{36,37} Aptamers represent another emerging strategy for the targeted delivery of RNA therapeutics.^{38,39} High affinity, target specificity, low immunogenicity and toxicity, short-term and low production costs, reproducibility from batch to batch, and smaller size than antibodies support aptamers as promising targeting molecules for systemic delivery.¹¹

Although cholesterol has been known to direct the conjugated-oligonucleotides to liver, we observed a major accumulation of our delivery platform into tumors instead of liver, indicating that our platform was directed to target

cells by the aptamer, but not to liver by the cholesterol. A potential explanation is that the cholesterol has formed a hydrophobic core that was inaccessible to cell surface cholesterol receptors. Notably, it would be difficult to use the negatively-charged oligonucleotide aptamers as targeting molecules for polycationic polymer-based delivery nanoparticles that electrostatically condense and hold negatively-charged oligonucleotides inside particles. This type of nanoparticle would physically inhibit the localization of aptamers on the surface during the process of particle self-assembly, which would likely interrupt the targeting capability of aptamers.^{38,39} In our platform, the cationic magnesium ions, electrostatically attracted to the strong anionic field around oligonucleotides,⁴⁰ would stabilize the particle structure through electrostatic interactions with the anionic oligonucleotides without interrupting the localization of aptamers on the particle surface. In addition, since magnesium ions generally support the conformational stability of aptamers,^{40,41} the magnesium ions would not interrupt the targeting capability of aptamers, which was demonstrated by the target-specific binding of the delivery platform (Fig. 2A). Our novel type of nanoparticle carrier using aptamers for targeting would further enhance the therapeutic potential of aptamers for targeted delivery of small RNA therapeutics.

Magnesium ions are known to increase the melting temperature of short RNA duplexes,^{40,41} which stabilizes the core component of our delivery platform assembled by the annealing 3 short RNA sequences. In combination with the rich 2'-fluoro RNA modifications, our platform provides better structural stability than FDA-approved micelle drugs.¹⁷ In contrast, the annealed short RNA duplexes (10–12 nt) would be disassembled through the acidification of endosomal trafficking due to the susceptibility of short RNA to denaturing under the acidic conditions,⁴² that would prompt the pH-sensitive disassembling of our delivery platform in the absence of magnesium.

While magnesium concentration in endosomes has not been reported, the concentration in plasma is 1.5–2 mM and its intracellular concentration is 0.5 mM.⁴³ Therefore, the plasma magnesium and neutral pH should help to stabilize the nanoparticles in the blood. Since the nanoparticles release magnesium in a pH-dependent manner, it would likely disassemble and expose cholesterol in the lysosome. The known effect of cholesterol on the membrane of endosomes and lysosomes and the impact of increased free magnesium on the osmotic balance of endosomes/lysosomes could provide a plausible explanation of the observed lysosomal disruption/leakiness and effective gene silencing by our delivery platform.^{17,19} Further investigations would be required.

Interestingly, we found that the miR-26a chimera significantly increased expression of a Th1 chemokine, Cxcl9 in tumors and peripheral blood. Recent studies demonstrated that Cxcl9 mediates the recruitment of T cells into tumors.⁴⁴ In breast cancer, Cxcl9 levels are significantly associated with lymphocyte infiltration.^{45–47} The T cell accumulation to tumor sites is significantly correlated with therapeutic efficiency of immune checkpoint inhibitors (ICIs).^{48,49} While elevation of Cxcl9 provides a plausible explanation for the increased T cell

recruitment, additional studies are needed to establish causality. Moreover, Ezh2-mediated histone modification has known to repress the expression of Cxcl9 in cancer cells, and subsequently decrease effector T-cell trafficking into tumor sites.^{23,50} Since Ezh2 is one of the miR-26a target genes, restoration of miR-26a in cancer cells by cancer-specific miR-26a delivery provided a valuable approach to increase T cell recruitment by reducing Ezh2-mediated repression of Cxcl9. Increased T cell recruitment potentiates immunotherapy, as demonstrated by our data using the anti-CTLA4 antibody as an example (Fig. S6). While additional studies are needed to fully describe the immunological mechanism of the combination therapy, our data provided herein show the potential of our nanoparticle to modify the tumor microenvironment to allow more effective immunotherapy.

Author contributions

Conception and design: T.T., Y.L. and M.D. Development of methodology: T.T., P.Z. and Y.L. Acquisition of data: T.T., W.I., C.B. and Y.W. Analysis and interpretation of data: T.T. and P.Z. Writing and review of manuscript: T.T., Y.L. and M.D. Study supervision: P.Z. and Y.L.

Conflict of interests

Y.L. and P.Z. are cofounders and have equity interest in OncoC4, Inc. M.D. has an equity interest in OncoC4, Inc.

Funding

This work was supported by grants from National Institutes of Health (No. R41OD028767) and Oncolmmune, Inc, which was acquired by Merck, Inc.

Acknowledgements

The electron microscopy was performed at the Electron Microscopy Core Imaging Facility in the Center for Innovative Biomedical Resources of the University of Maryland, Baltimore, supported by Dr. Ru-Ching Hsia.

Appendix A. Supplementary data

Supplementary data to this article can be found online at <https://doi.org/10.1016/j.gendis.2022.05.004>.

References

- Kaczmarek JC, Kowalski PS, Anderson DG. Advances in the delivery of RNA therapeutics: from concept to clinical reality. *Genome Med.* 2017;9(1):60.
- Davidson BL, McCray Jr PB. Current prospects for RNA interference-based therapies. *Nat Rev Genet.* 2011;12(5):329–340.
- Bobbin ML, Rossi JJ. RNA interference (RNAi)-based therapeutics: delivering on the promise? *Annu Rev Pharmacol Toxicol.* 2016;56:103–122.
- Daka A, Peer D. RNAi-based nanomedicines for targeted personalized therapy. *Adv Drug Deliv Rev.* 2012;64(13):1508–1521.
- Dowdy SF. Overcoming cellular barriers for RNA therapeutics. *Nat Biotechnol.* 2017;35(3):222–229.
- Johannes L, Lucchino M. Current challenges in delivery and cytosolic translocation of therapeutic RNAs. *Nucleic Acid Therapeut.* 2018;28(3):178–193.
- Setten RL, Rossi JJ, Han SP. The current state and future directions of RNAi-based therapeutics. *Nat Rev Drug Discov.* 2019;18(6):421–446.
- Hu B, Zhong L, Weng Y, et al. Therapeutic siRNA: state of the art. *Signal Transduct Targeted Ther.* 2020;5(1):101.
- Saw PE, Song EW. siRNA therapeutics: a clinical reality. *Sci China Life Sci.* 2020;63(4):485–500.
- Juliano RL. The delivery of therapeutic oligonucleotides. *Nucleic Acids Res.* 2016;44(14):6518–6548.
- Bouchard PR, Hutabarat RM, Thompson KM. Discovery and development of therapeutic aptamers. *Annu Rev Pharmacol Toxicol.* 2010;50:237–257.
- Zhao N, Pei SN, Qi J, et al. Oligonucleotide aptamer-drug conjugates for targeted therapy of acute myeloid leukemia. *Biomaterials.* 2015;67:42–51.
- Zhang Y, Huo M, Zhou J, et al. PKSolver: an add-in program for pharmacokinetic and pharmacodynamic data analysis in Microsoft Excel. *Comput Methods Progr Biomed.* 2010;99(3):306–314.
- Tanno T, Zhang P, Lazarski CA, et al. An aptamer-based targeted delivery of miR-26a protects mice against chemotherapy toxicity while suppressing tumor growth. *Blood Adv.* 2017;1(15):1107–1119.
- Ercole F, Whittaker MR, Quinn JF, et al. Cholesterol modified self-assemblies and their application to nanomedicine. *Bio-macromolecules.* 2015;16(7):1886–1914.
- Lipfert J, Doniach S, Das R, et al. Understanding nucleic acid-ion interactions. *Annu Rev Biochem.* 2014;83:813–841.
- Bissery MC, Nohynek G, Sanderink GJ, et al. Docetaxel (Taxotere): a review of preclinical and clinical experience. Part I: preclinical experience. *Anti Cancer Drugs.* 1995;6(3):339–355, 363–368.
- Wang S, Allen N, Liang XH, et al. Membrane destabilization induced by lipid species increases activity of phosphorothioate-antisense oligonucleotides. *Mol Ther Nucleic Acids.* 2018;13:686–698.
- Bhakta G, Shrivastava A, Maitra A. Magnesium phosphate nanoparticles can be efficiently used in vitro and in vivo as non-viral vectors for targeted gene delivery. *J Biomed Nanotechnol.* 2009;5(1):106–114.
- Johnson DE, Ostrowski P, Jaumouillé V, et al. The position of lysosomes within the cell determines their luminal pH. *J Cell Biol.* 2016;212(6):677–692.
- Wittrup A, Lieberman J. Knocking down disease: a progress report on siRNA therapeutics. *Nat Rev Genet.* 2015;16(9):543–552.
- Harris JM, Chess RB. Effect of pegylation on pharmaceuticals. *Nat Rev Drug Discov.* 2003;2(3):214–221.
- Peng D, Kryczek I, Nagarsheth N, et al. Epigenetic silencing of TH1-type chemokines shapes tumour immunity and immunotherapy. *Nature.* 2015;527(7577):249–253.
- Harlin H, Meng Y, Peterson AC, et al. Chemokine expression in melanoma metastases associated with CD8⁺ T-cell recruitment. *Cancer Res.* 2009;69(7):3077–3085.
- Longmire M, Choyke PL, Kobayashi H. Clearance properties of nano-sized particles and molecules as imaging agents: considerations and caveats. *Nanomedicine.* 2008;3(5):703–717.
- Kore G, Kolate A, Nej A, et al. Polymeric micelle as multi-functional pharmaceutical carriers. *J Nanosci Nanotechnol.* 2014;14(1):288–307.

27. Yin W, Rogge M. Targeting RNA: a transformative therapeutic strategy. *Clin Transl Sci.* 2019;12(2):98–112.
28. Braasch DA, Jensen S, Liu Y, et al. RNA interference in mammalian cells by chemically-modified RNA. *Biochemistry.* 2003;42(26):7967–7975.
29. Crooke ST, Wang S, Vickers TA, et al. Cellular uptake and trafficking of antisense oligonucleotides. *Nat Biotechnol.* 2017;35(3):230–237.
30. Khvorova A, Watts JK. The chemical evolution of oligonucleotide therapies of clinical utility. *Nat Biotechnol.* 2017;35(3):238–248.
31. Brown DA, Kang SH, Gryaznov SM, et al. Effect of phosphorothioate modification of oligodeoxynucleotides on specific protein binding. *J Biol Chem.* 1994;269(43):26801–26805.
32. Sioud M. RNA interference and innate immunity. *Adv Drug Deliv Rev.* 2007;59(2–3):153–163.
33. Yee NS, Hsiao CW, Serve H, et al. Mechanism of down-regulation of c-kit receptor. Roles of receptor tyrosine kinase, phosphatidylinositol 3'-kinase, and protein kinase C. *J Biol Chem.* 1994;269(50):31991–31998.
34. Miettinen M, Lasota J. KIT (CD117): a review on expression in normal and neoplastic tissues, and mutations and their clinicopathologic correlation. *Appl Immunohistochem. Mol Morphol.* 2005;13(3):205–220.
35. Rajeev KG, Nair JK, Jayaraman M, et al. Hepatocyte-specific delivery of siRNAs conjugated to novel non-nucleosidic trivalent N-acetylgalactosamine elicits robust gene silencing in vivo. *Chembiochem.* 2015;16(6):903–908.
36. Kumar P, Ban HS, Kim SS, et al. T cell-specific siRNA delivery suppresses HIV-1 infection in humanized mice. *Cell.* 2008;134(4):577–586.
37. Cuellar TL, Barnes D, Nelson C, et al. Systematic evaluation of antibody-mediated siRNA delivery using an industrial platform of THIOMAB-siRNA conjugates. *Nucleic Acids Res.* 2015;43(2):1189–1203.
38. Zhou J, Rossi JJ. Cell-type-specific, aptamer-functionalized agents for targeted disease therapy. *Mol Ther Nucleic Acids.* 2014;3(6):e169.
39. Dassie JP, Giangrande PH. Current progress on aptamer-targeted oligonucleotide therapeutics. *Ther Deliv.* 2013;4(12):1527–1546.
40. Misra VK, Draper DE. On the role of magnesium ions in RNA stability. *Biopolymers.* 1998;48(2–3):113–135.
41. Owczarzy R, Moreira BG, You Y, et al. Predicting stability of DNA duplexes in solutions containing magnesium and monovalent cations. *Biochemistry.* 2008;47(19):5336–5353.
42. Mariani A, Bonfio C, Johnson CM, et al. pH-driven RNA strand separation under prebiotically plausible conditions. *Biochemistry.* 2018;57(45):6382–6386.
43. de Rouffignac C, Quamme G. Renal magnesium handling and its hormonal control. *Physiol Rev.* 1994;74(2):305–322.
44. Rossi D, Zlotnik A. The biology of chemokines and their receptors. *Annu Rev Immunol.* 2000;18:217–242.
45. Denkert C, Loibl S, Noske A, et al. Tumor-associated lymphocytes as an independent predictor of response to neoadjuvant chemotherapy in breast cancer. *J Clin Oncol.* 2010;28(1):105–113.
46. Walsler TC, Ma X, Kundu N, et al. Immune-mediated modulation of breast cancer growth and metastasis by the chemokine Mig (CXCL9) in a murine model. *J Immunother.* 2007;30(5):490–498.
47. Chheda ZS, Sharma RK, Jala VR, et al. Chemoattractant receptors BLT1 and CXCR3 regulate antitumor immunity by facilitating CD8+ T cell migration into tumors. *J Immunol.* 2016;197(5):2016–2026.
48. Sharma P, Wagner K, Wolchok JD, et al. Novel cancer immunotherapy agents with survival benefit: recent successes and next steps. *Nat Rev Cancer.* 2011;11(11):805–812.
49. Du X, Tang F, Liu M, et al. A reappraisal of CTLA-4 checkpoint blockade in cancer immunotherapy. *Cell Res.* 2018;28(4):416–432.
50. Nagarsheth N, Peng D, Kryczek I, et al. PRC2 epigenetically silences Th1-type chemokines to suppress effector T-cell trafficking in colon cancer. *Cancer Res.* 2016;76(2):275–282.